Journal of
Materials Chemistry A

PAPER

Cite this: *J. Mater. Chem. A*, 2016, **4**, 18008

Highly efficient metal-free electrocatalysts toward oxygen reduction derived from carbon nanotubes@polypyrrole core–shell hybrids†

Hongli An, Ruikang Zhang, Zhenhua Li, Lei Zhou, Mingfei Shao* and Min Wei*

Received 13th October 2016
Accepted 24th October 2016

DOI: 10.1039/c6ta08892a

www.rsc.org/MaterialsA

Nitrogen-doped carbon nanotubes (NCNTs) are recognized as one of the most promising oxygen reduction reaction (ORR) catalysts, while developing a preparation protocol for CNT-based ORR catalysts with cost-effective synthesis, high activity and durability is still a challenge. In this work, we report the fabrication of N-doped CNT catalysts with a homogeneous distribution of dopants in the CNT matrix by pyrolysis of a core–shell nanostructured CNTs@polypyrrole nanocomposite (CNTs@PPy). The as-obtained NCNTs exhibit excellent performance in electrocatalytic oxygen reduction with an onset potential of 0.95 V *vs.* RHE, a diffusion-limited current of 6.82 mA cm^{-2} and excellent stability in alkaline media, much superior to that of reported CNT-based ORR catalysts as well as commercial Pt/C. Moreover, the ratio of different nitrogens (pyridinic, pyrrolic and graphitic N) can be tuned easily by changing the coating amount of PPy in the CNTs@PPy core–shell precursors; and the results indicate that the pyridinic-N in the CNTs@PPy derived NCNTs plays a key role in promoting the ORR performances.

Introduction

The oxygen reduction reaction (ORR) is a key process in energy storage and conversion systems including fuel cells and metal–air batteries.[1,2] Noble metals (*e.g.*, Pt, Pd, Ru, *etc.*) and their alloy nanoparticles have been widely used as ORR electrocatalysts with high activity,[3–7] but the high cost, low poison resistance and unsatisfactory durability limit their widespread applications. To overcome this issue, inexpensive ORR catalysts including nonprecious metal- and metal-free catalysts have been intensively explored,[8–13] among which heteroatom (*e.g.*, N, B, P, Co, and Fe)-doped carbon materials showed satisfactory electrocatalytic behavior with excellent conductivity and anti-corrosion properties.[14–19] Recently, several methods have been developed to promote the performances of carbon-based ORR catalysts, *via* tuning the intrinsic active sites or constructing nanostructures with an improved surface area and electron/mass transportation.[20–22] In spite of all these progresses, achieving sufficient carbon-based ORR catalysts with a fine control over dopants and architecture is still a huge challenge.

Carbon nanotubes (CNTs) take advantage of their large surface area, excellent electrical conductivity and extraordinarily high anti-corrosion properties.[23,24] Recently, nitrogen-doped carbon nanotubes (NCNTs) have been recognized as one of the most promising ORR catalysts.[25–29] Two preparation routes, including the *in situ* doping and the post-treatment of CNTs with nitrogen precursors (*e.g.*, NH_3 and pyridine),[30,31] have been mainly explored for the synthesis of NCNTs. However, for a given strategy, it is practically hard to simultaneously achieve sufficient doping and a sophisticated nanostructure due to some intrinsic limitations of individual constitution. For instance, the *in situ* doping method benefits from a uniform heteroatom distribution but suffers from rigorous conditions and reproducibility. In contrast, the post-treatment route normally shows a facile operation but is limited by inhomogeneous doping and reactant corrosiveness. Thus, developing a facile and effective approach to prepare N-doped CNT electrocatalysts toward the ORR with a hierarchical nanostructure and desirable doping simultaneously remains a challenge.

Herein, we report the preparation of a N-doped CNT material *via* a facile two-step route: synthesis of a CNTs@polypyrrole (PPy) composite with a core–shell structure, followed by a further pyrolysis treatment at 800 °C for homogeneous N doping. The resulting product (denoted as CNTs@PPy-P800) provides a hierarchical mesoporous structure (mainly centered at 2–3 nm and 30–40 nm) with a uniform N doping of 6.90 at% in the graphite carbon matrix. The homogeneously doped nitrogen in the matrix of CNTs with excellent electrical conductivity and anti-corrosion properties offers active sites for the ORR. Moreover, the hierarchical porous nanostructure provides ion transport channels, which facilitates the mass diffusion in the ORR. Particularly, CNTs@PPy-P800 exhibits a promising ORR performance, with an onset potential of 0.95 V *vs.* RHE and a diffusion-limited current of 6.82 mA cm^{-2}, much

---

State Key Laboratory of Chemical Resource Engineering, Beijing University of Chemical Technology, Beijing 100029, P. R. China. E-mail: shaomf@mail.buct.edu.cn; weimin@mail.buct.edu.cn; Fax: +86-10-64425385; Tel: +86-10-64412131

† Electronic supplementary information (ESI) available. See DOI: 10.1039/c6ta08892a

superior to that of the commercial Pt/C catalyst. To the best of our knowledge, the diffusion-limited current density afforded by CNTs@PPy-P800 is also larger than that of previously reported N-CNT catalysts in alkaline media. In addition, the CNTs@PPy-P800 catalyst shows a long-term durability and strong tolerance against methanol crossover for electrocatalytic oxygen reduction. This work provides a new strategy for the preparation of N-doped CNTs, which can serve as a promising metal-free ORR catalyst in fuel cells and metal–air batteries.

Experimental section

Materials

Pyrrole (AR, 99%) and $(NH_4)_2S_2O_8$ (AR, 99%) were purchased from Aladdin Reagent Co. Ltd. HNO_3 (AR, 65%) was obtained from Beijing Chemical Co. Ltd. Deionized water was used in all the experimental processes.

Synthesis of CNTs@PPy-P800

CNTs used in this work were synthesized by ethylene cracking on ceramic spheres through a floating catalysis process.[32] For the chemical modification of the CNT surface, the CNT (0.6 g) sample was refluxed in HNO_3 (65 wt%, 90 mL) at 100 °C for 5 h, followed by washing thoroughly with deionized water, and dried at 60 °C for further use. Synthesis of the CNTs@PPy composite with a core–shell structure: the pre-treated CNTs (0.128 g) were dispersed in deionized water (100 mL) by ultra-sonication for 30 min, followed by addition of a pyrrole monomer (0.4 mL). Subsequently, the $(NH_4)_2S_2O_8$ solution (0.115 M, 100 mL) was added dropwise into the mixed suspension with magnetic stirring, aging at room temperature for 12 h. The resulting product was filtered, washed thoroughly and finally dried at 60 °C in air. In the case of optimization experiments, the pyrrole volume was changed to 0.05, 0.2, 0.4 and 0.6 mL, respectively. Synthesis of CNTs@PPy-P800: the as-prepared CNTs@PPy was placed in a ceramic boat and transferred into a temperature-programmed furnace. The pyrolysis treatment was performed at 800 °C for 2 h with a heating rate of 5 °C min^{-1} in a N_2 atmosphere.

Characterization

X-ray diffraction patterns were collected on a Shimadzu XRD-6000 diffractometer using a Cu Kα source, with a scan step of 0.02° and a scan range between 3° and 70°. X-ray photoelectron spectra (XPS) were recorded on a Thermo VG ESCALAB 250 X-ray photoelectron spectrometer at a pressure of 2×10^{-9} Pa using Al Kα X-rays as the excitation source. The specific surface area determination, pore volume and size analysis were performed by the Brunauer–Emmett–Teller (BET) and Barrett–Joyner–Halenda (BJH) methods, respectively, using a Quantachrome Autosorb-1CVP analyzer. Prior to the measurements, the samples were degassed at 150 °C for 8 h. The morphology was investigated using a scanning electron microscope (SEM; Zeiss SUPRA 55) with an accelerating voltage of 20 kV, combined with energy dispersive X-ray spectroscopy for the determination of carbon-based materials. Transmission electron microscope (TEM) images were recorded using a Philips Tecnai 20 and JEOL JEM-2010 high-resolution transmission electron microscopes with an accelerating voltage of 200 kV in each case.

Electrochemical measurements

Electrochemical measurements were performed on a CHI 760E electrochemical workstation (Instruments, Chenhua Co., China) in a conventional three-electrode cell, with a platinum wire as the counter electrode, a Ag/AgCl as the reference electrode, and a catalyst-modified glassy carbon electrode (GCE) as the working electrode. A rotating disk electrode (RDE: 3.0 mm in diameter) and rotating ring-disk electrode (RRDE: 5.61 mm in diameter) were used as the substrate for the working electrode. Prior to use, the RDE and RRDE were polished with aqueous alumina suspensions using felt polishing pads and washed with deionized water and ethanol. The catalyst ink was prepared by adding the catalyst (2 mg) into a solution containing 780 μL of deionized water, 200 μL of ethanol and 20 μL of 5 wt% Nafion solution to form a homogeneous suspension (catalyst concentration: 2 mg mL^{-1}). A calculated amount (7 μL) of the suspension was then evenly cast on the clean GCE surface with a syringe and dried in air, corresponding to a catalyst loading of 0.2 mg cm^{-2}, including the commercial Pt/C catalyst (20 wt% of Pt). Before testing, a N_2 or O_2 flow was used for the electrolyte in the cell for 30 min to give a saturation state. Cyclic voltammetry (CV) experiments were performed in N_2- and O_2-saturated 0.1 M KOH solution at a scan rate of 10 mV s^{-1}. Linear sweep voltammograms (LSV) were acquired in an O_2-saturated 0.1 M KOH solution at various rotation rates (625–2500 rpm). RRDE measurements were also conducted in O_2-saturated 0.1 M KOH at room temperature. The stability tests were carried out at 0.5 V in O_2-saturated 0.1 M KOH (ω = 1600 rpm) by the chronoamperometric method. The electron transfer number and the peroxide percentage can be further calculated by the following equations:

$$n = 4 \times \frac{i_d}{i_r/N + i_d} \tag{1}$$

$$\%\,HO_2^- = 200 \times \frac{i_r/N}{i_r/N + i_d} \tag{2}$$

where i_d is the disk current; i_r is the ring current and N is the current collection efficiency of the Pt ring ($N = 0.37$).

The measured potentials *vs.* Ag/AgCl reference electrode were converted to the reversible hydrogen electrode (RHE) scale *via* the Nernst equation:

$$E_{RHE} = E_{Ag/AgCl} + 0.059\ pH + E^0_{Ag/AgCl} \tag{3}$$

where E_{RHE} is the converted potential *vs.* RHE; $E_{Ag/AgCl}$ is the experimental potential measured against the Ag/AgCl reference electrode, and $E^0_{Ag/AgCl}$ is the standard potential of Ag/AgCl at 25 °C (0.197 V). The electrochemical measurements were carried out in 0.1 M KOH (pH = 13) at room temperature; therefore:

$$E_{RHE} = E_{Ag/AgCl} + 0.964\ V \tag{4}$$

Results and discussion

The synthesis process of N-doped CNTs by pyrolysis of the core–shell CNTs@PPy composite is illustrated in Scheme 1. First, the CNT precursor (diameter: 15–25 nm, wall thickness: $\sim$5 nm; Fig. 1a) was mixed with a pyrrole monomer with vigorous stirring, followed by dropwise addition of ammonium persulfate solution to induce the *in situ* polymerization of pyrrole on the surface of CNTs. After coating with PPy, the CNTs show a rough surface (Fig. S1a and b†). The high resolution transmission electron microscope (HRTEM) images of CNTs@PPy display a typical core–shell structure with a uniform thin layer of PPy (2–3 nm) on the surface of CNTs (Fig. 1b). Subsequently, the as-obtained CNTs@PPy composite was subjected to a pyrolysis treatment in a N_2 atmosphere at 800 °C. The resulting product CNTs@PPy-P800 shows a smaller diameter (20–30 nm) than the CNTs@PPy precursor due to volume shrinkage with the release of non-carbon elements of PPy during the carbonization (Fig. 1d and S1d†). In contrast, the morphology of pristine CNTs after the same pyrolysis process (CNTs-P800) does not display any change (Fig. 1c and S1c†). For the sample of CNTs@PPy-P800, the electron energy loss spectroscopy (EELS) measurements demonstrate that the element C is mainly distributed in the CNT walls, accompanied by a homogeneous distribution of N throughout the carbon shell (Fig. 1e–g), indicating a successful doping of N into the CNT matrix. The powder X-ray diffraction (XRD) pattern of CNTs-P800 contains two characteristic peaks at $2\theta \sim 26°$ and 44° (Fig. S2a†), corresponding to the (002) and (101) reflection of the graphite structure, respectively.[33] The XRD pattern of PPy-P800 only shows a broad peak at $\sim$15°, indicating its amorphous structure. In the case of the CNTs@PPy-P800 sample, a superimposition of a CNTs-P800 phase and a PPy-P800 phase is observed, suggesting the carbonization of a PPy layer on the surface of CNTs. Raman spectroscopy was used to further study the structure of CNTs-P800, PPy-P800 and CNTs@PPy-P800, which confirms the presence of a CNTs-P800 phase and a PPy-P800 phase. Both the CNTs@PPy-P800 and CNTs-P800 display rather similar Raman spectra (Fig. S2b†): the G band at 1590 cm^{-1} and D band at 1335 cm^{-1} are clearly resolved, which gives strong evidence for the formation of graphitized carbon.[34] The XPS spectrum of CNTs@PPy-P800 reveals signals of C, N and O elements with a content of 88.5 at%, 6.90 at% and 4.59 at%, respectively. And the XPS spectrum of PPy-P800 reveals signals of C, N and O elements with a content of 84.85 at%, 5.67 at% and 9.48 at%, respectively (Fig. S2c, d and Table S7†). The content of N in the CNTs@PPy-P800 sample increases, indicating a successful doping of N into the CNT matrix. High resolution scans of C 1s were used to further analyze the PPy-P800 and CNTs@PPy-P800. The C 1s spectrum can be deconvoluted into four peaks at 284.6, 285.5, 287.2 and 288.8 eV (Fig. S3†), corresponding to C=C, C–C, C–N, and C–O, respectively (Table S1†). The CNTs@PPy-P800 sample shows an obviously increased content of C–N (10.73%) compared with PPy-P800 (5.64%), indicating a successful doping of N into the CNT matrix.

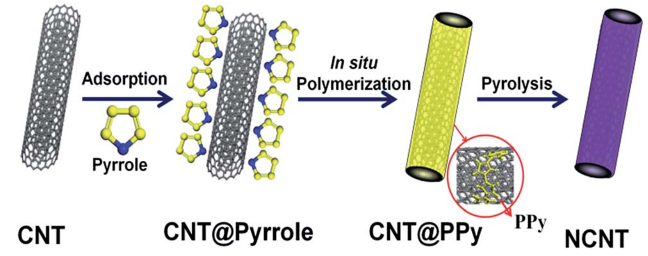

Scheme 1 Schematic illustration of the synthesis of N-doped CNTs.

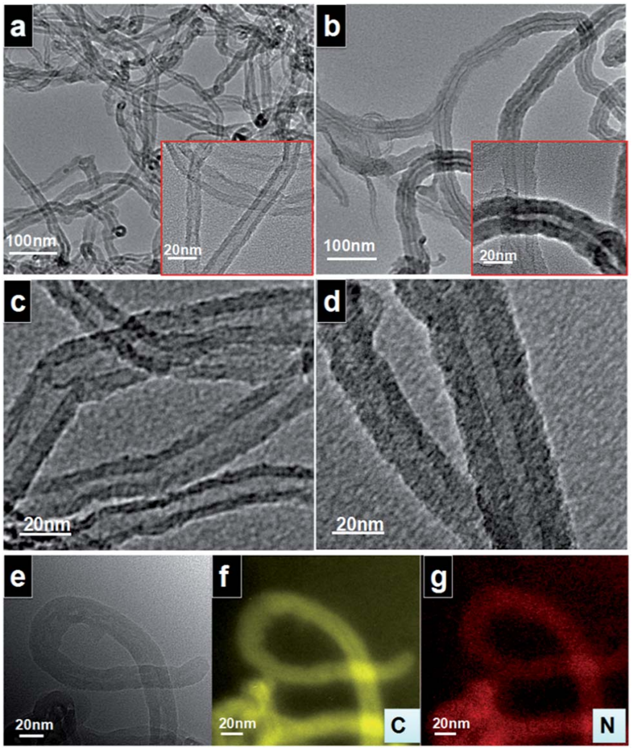

Fig. 1 HRTEM images of (a) CNTs, (b) CNTs@PPy, (c) CNTs-P800 and (d) CNTs@PPy-P800, respectively. (e) A typical TEM image of CNTs@PPy-P800 and the corresponding EELS mappings of elements C (f) and N (g).

The ORR catalytic activities of CNTs@PPy-P800 and the corresponding reference samples are studied in alkaline media with a mass loading of $\sim$0.2 mg cm^{-2}. All potentials are calibrated to a reversible hydrogen electrode (RHE). As shown in cyclic voltammetry (CV) curves (Fig. 2a), the CNTs@PPy-P800 electrode shows a much stronger cathodic peak in O_2-saturated solution than that in a N_2-saturated electrolyte, indicating its significant ORR activity. The ORR performance studied by linear sweep voltammetry (LSV) shows that the CNTs@PPy-P800 derived from LSV plots is 6.82 mA cm^{-2} at 0.2 V. CNTs@PPy-P800 exhibits a more positive potential as well as larger diffusion-limited current density (Fig. 2b), superior to those of PPy-P800, CNTs-P800 and the commercial Pt/C catalyst.

As shown in Fig. 2c and Table S2,† the onset potential of CNTs@PPy-P800 is 0.95 V (*vs.* RHE), more positive in comparison with PPy-P800 (0.78 V), CNTs-P800 (0.82 V) and the commercial Pt/C catalyst (0.94 V). The half-wave potential of

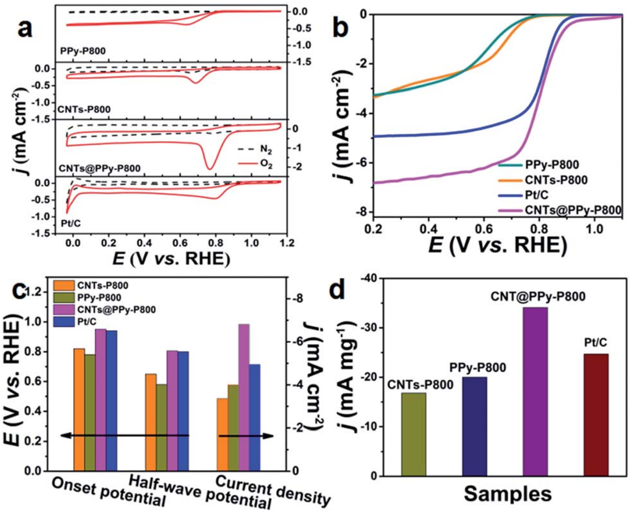

Fig. 2 (a) CV curves of PPy-P800, CNTs-P800, CNTs@PPy-P800 and Pt/C in N_2 and O_2-saturated solution, respectively. (b) LSV curves of PPy-P800, CNTs-P800, CNTs@PPy-P800 and Pt/C catalyst in O_2-saturated 0.1 M KOH solution at a sweep rate of 10 mV s^{-1} and an electrode rotation speed of 1600 rpm. (c) The onset potential, half-wave potential, and current density of PPy-P800, CNTs-P800, CNTs@PPy-P800 and Pt/C, respectively. (d) Corresponding mass activities of these four samples.

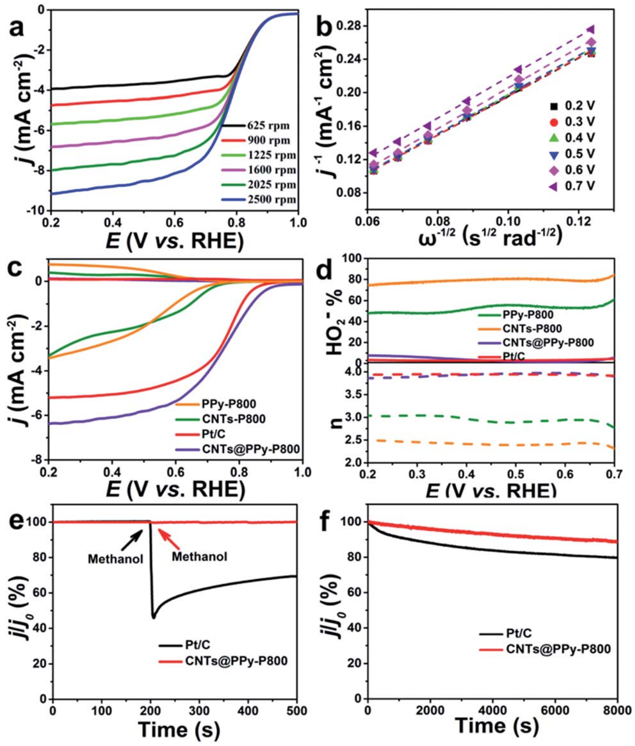

Fig. 3 (a) LSV curves of CNTs@PPy-P800 at the rotation rate from 625 to 2500 rpm. (b) Corresponding K–L plots derived from the RDE data. (c) RRDE curves of CNTs-P800, PPy-P800, CNTs@PPy-P800 and the Pt/C catalyst. The disk current densities (bottom) and ring current densities (top) are displayed separately with the rotating speed of 1600 rpm. (d) Peroxide yield (solid line) and electron transfer number (n, dash line) of CNTs-P800, PPy-P800, CNTs@PPy-P800 and the Pt/C catalyst at various potentials based on the RRDE data. I–t curves of CNTs@PPy-P800 and Pt/C in O_2-saturated 0.1 M KOH solution: (e) without and with 1.0 M methanol; (f) long-term stability.

CNTs@PPy-P800 is 0.81 V, ~160 mV more positive than that of CNTs-P800 (0.65 V) and 230 mV more positive than that of PPy-P800 (0.58 V). In addition, the limiting current density of CNTs@PPy-P800 is much larger than that of CNTs-P800 (3.36 mA cm^{-2}), PPy-P800 (4.0 mA cm^{-2}) and the commercial Pt/C (4.94 mA cm^{-2}), further demonstrating the excellent activity of CNTs@PPy-P800 toward the ORR. It is worth mentioning that this limiting current density, to the best of our knowledge, is also superior to that of other reported N-CNT based catalysts (Table S10†). The electrocatalytic performance using an electrode with a large CNTs@PPy-P800 loading was also studied, which demonstrated a superior activity to that of the Pt/C electrode (Fig. S4a and Table S3†). To better demonstrate the catalytic activity of these four catalysts, their mass activities are also obtained (Fig. S4b† and 2d). As shown in Fig. 2d, the limiting current density of CNTs@PPy-P800 is 34.1 mA mg^{-1} at 0.2 V, significantly higher than that of PPy-P800 (20 mA mg^{-1}), CNTs-P800 (16.8 mA mg^{-1}) and the commercial Pt/C catalyst (24.7 mA mg^{-1}). The SCN^- ions were usually introduced into the electrolyte to strongly coordinate and poison iron-based catalytic sites if any.[35] Herein, no activity loss of the CNTs@PPy-P800 electrode is observed after the addition of KSCN (Fig. S5†), illustrating the high intrinsic activity of this novel metal-free NCNT catalyst.

The rotating disk electrode (RDE) measurements at various rotating speeds at a scan rate of 10 mV s^{-1} in an O_2-saturated system are carried out and the Koutecky–Levich (K–L) equation is used to study the kinetic parameters (Fig. 3a and b). The limiting current density of the CNTs@PPy-P800 electrode increases along with the increase of rotation speed from 625 to 2500 rpm. The corresponding K–L plots within the potential range 0.2–0.7 V exhibit a good linearity with a rather consistent slope, suggesting the first order reaction kinetics of the ORR with respect to the oxygen concentration in the solution. The electron transfer number (n) was calculated to be 3.72–3.94 within 0.2–0.7 V, indicating a 4e ORR process catalyzed by CNTs@PPy-P800, similar to the Pt/C catalyst (Fig. S6f†). In contrast, the PPy-P800 and CNTs-P800 electrodes with poor electrocatalytic selectivity only give a much lower electron transfer number of 3.03–3.27 and 1.32–2.89 (Fig. S6†), respectively. To further quantify the ORR pathway, a rotation ring-disk electrode (RRDE) is used to monitor the formation of HO_2^- during the ORR process (Fig. 3c and d). The HO_2^- yield of CNTs@PPy-P800 is below 7.6% and the value of n ranges from 3.86 to 3.97, also close to Pt/C and consistent with the results obtained from the K–L plots based on the RDE study. However for the CNTs-P800 electrode, the HO_2^- yield reaches ~50% and n ranges from 2.77 to 3.03; the HO_2^- yield for PPy-P800 even reaches as high as ~85% (n: 2.30–2.50), both of which indicate a two-electron transfer pathway in the oxygen reduction process. In addition to the activity, the stability is another key aspect for high-performance ORR catalysts. The chronoamperometric (CA) measurement is performed to test the possible crossover effect caused by methanol for CNTs@PPy-P800 and the commercial Pt/C catalyst. As depicted in Fig. 3e, when 1.0 M methanol is added into the O_2-saturated 0.1 M KOH solution, the Pt/C electrode shows a sharp decrease in current density; while no obvious loss is observed for the CNTs@PPy-P800 electrode, suggesting its strong tolerance against methanol. The durability of the CNTs@PPy-P800 and commercial Pt/C catalyst was then tested by CA measurements at 0.50 V in an O_2-saturated 0.1 M KOH solution. After 8000 s of continuous operation, the commercial Pt/C electrode displays a sharp decrease in voltammetric current by ~20%; whereas the CNTs@PPy-P800 catalyst retains up to 92% of its original current under the same experimental conditions (Fig. 3f). This clearly demonstrates the superior stability of the CNTs@PPy-P800 catalyst toward the ORR.

It is reported that the pyrolysis temperature plays a key role in the synthesis of carbon-based ORR electrocatalysts,[36,37] which was therefore investigated (denoted as CNTs@PPy-*T*; *T* is the temperature). As shown in Fig. S7a and Table S4,† the ORR performance of CNTs@PPy-*T* improves gradually with the increase of pyrolysis temperature from 600 °C to 800 °C, and then decreases with a further increase of temperature to 900 °C. The XPS spectra of these four samples CNTs@PPy-*T* ($T = 600$, 700, 800 and 900 °C) were measured to study the chemical state of N-doping. The N 1s spectrum can be deconvoluted into three peaks at 398.4, 399.8 and 400.9 eV (Fig. S8a†), which are ascribed to pyridinic N, pyrrolic N and graphitic N (denoted as pyri-N, pyrr-N and grap-N, respectively).[38] As the pyrolysis temperature increases, the relative content of pyrr-N species reduces gradually whilst that of grap-N increases significantly. The summation of pyri-N and grap-N shows an increase to a maximum of 88.11% at 800 °C (Fig. S8b and Table S5†), which is consistent with the trend of ORR activity of CNTs@PPy-*T* samples. The results above indicate that pyridinic N and graphitic N play a crucial role in the ORR activity, in accordance with the previous reports.[39,40]

The influence of the coating amount of PPy on the produced NCNT products is further studied. Four samples of CNTs@PPy with various contents of PPy are synthesized by controlling the pyrrole volume (0.05 mL, 0.2 mL, 0.4 mL and 0.6 mL, respectively) during the precursor synthesis. After pyrolysis treatment, the resulting CNTs@PPy-P800 products (denoted as NCNT-1, NCNT-2, NCNT-3 and NCNT-4, respectively) give a rather similar morphology and core–shell structure (Fig. S9†). However, the thickness of the carbon shell on the surface of CNTs shows a gradual increase from 5.48 nm to 7.10 nm along with the increase of PPy in the precursors (Fig. 4a). Their ORR performance was further investigated by LSV (Fig. S7b†), from which it is clear that NCNT-3 exhibits the most positive onset potential and half-wave potential as well as the largest diffusion-limited current density among these samples (Fig. 4b and Table S6†). It has been reported that the N doping amount and the type of N species are two key parameters in the ORR process.[41,42] Fig. 4c shows the total nitrogen content of these four samples determined by XPS, which gives increasing values from 2.06 at% to 7.89 at% (Table S7†). This demonstrates that a higher N content in the CNTs does not always contribute to the improvement of the ORR performance. The N 1s spectra of all these CNTs@PPy-P800 samples can be mainly deconvoluted into pyri-N (398.4 eV), pyrr-N (399.8 eV) and grap-N (400.9 eV), and their relative contents are shown in Fig. S10 (inset) and Table S8.† The pyri-N shows an obvious increase from 9.68% to 36.58% with the enhancement of a carbon shell thickness from 5.48 nm to 6.45 nm, followed by a decline for the sample of NCNT-4 (22.92%); however, the grap-N displays a gradual decrease from 67.47% to 51.53%, followed by an increase for the sample of NCNT-4 (65.17%). It's interesting that the summation of pyri-N and grap-N shows a maximum of 88.11% for the sample of NCNT-3, in accordance with the highest ORR activity. This indicates that pyri-N and grap-N act as active sites but pyri-N contributes dominantly toward the ORR.[43]

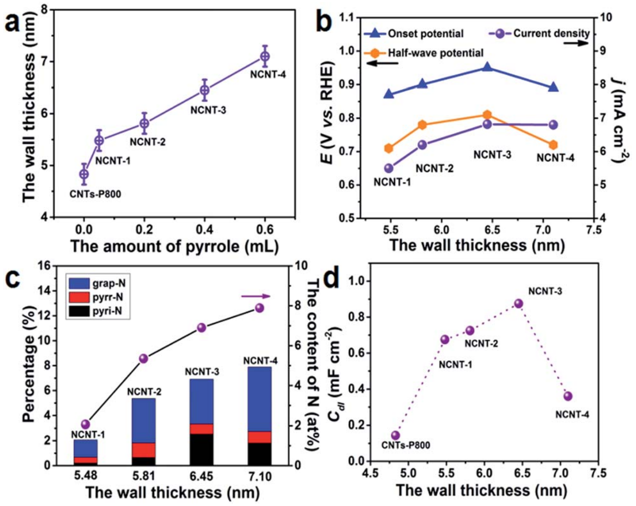

Fig. 4 (a) Wall thickness of NCNT catalysts. (b) Onset potential, half-wave potential, and current density of NCNT-*x* samples ($x = 1$, 2, 3 and 4, respectively). (c) Percentage of various nitrogen species of NCNT-*x* samples. (d) Double layer capacitance C_{dl} of NCNT-*x*, which is used to represent the ECSA.

The electrochemical impedance spectroscopy (EIS) measurements in the ORR region at 1.06 V *vs.* RHE are conducted[44] and the corresponding Nyquist plots of the EIS spectra are shown in Fig. S11.† It is found that all these CNTs@PPy derived catalysts display a semicircle in the high frequency region and a straight line in the low frequency region. The NCNT-3 shows a smaller semicircle diameter and a larger slope than other samples, implying its faster electron transport kinetics and ion diffusion rate. The electrochemically active surface area (ECSA) estimated from the double-layer capacitance (C_{dl}) of the electrode surface is measured to reveal the intrinsic activity (Fig. 4d). The linear slope of capacitive current *vs.* scan rate, equivalent to twice the double-layer capacity C_{dl}, is used to represent the ECSA (Fig. S12†). It is found that all these NCNTs show a higher ECSA value than that of non-doped CNTs, illustrating a largely improved ORR activity by introducing N atoms into the CNT matrix. In the cases of four N-doping samples, the ECSA value increases first for NCNT-1 to NCNT-3, and then decreases for NCNT-4. This is highly consistent with the trend of the pyri-N content, which further indicates that pyri-N plays a key role in promoting the ORR process. Taking into account the mass diffusion, the surface area and pore-size distribution of these samples are further investigated. Based on the Barrett–Joyner–Halenda (BJH) model, all these NCNT samples exhibit a broad pore diameter distribution centered at 2–3 nm and 30–40 nm, corresponding to a hierarchical mesoporous nature (Fig. S13b†). However, the specific surface area of NCNT materials shows a gradual decrement from 192.47 $m^2 g^{-1}$ to 149.46 $m^2 g^{-1}$ with the increase of N-doping (Fig. S13a and Table S9†). The results above indicate that a suitable N-doping improves the intrinsic activity of CNTs toward the ORR; whilst over-doping reduces the specific surface area of the catalyst and limits the exposure of active sites.

Conclusions

In summary, we developed a facile and effective synthetic approach to prepare N doped CNTs as efficient ORR electrocatalysts by pyrolysis of the CNTs@PPy composite. The as-obtained CNTs@PPy-P800 catalyst with a uniform N doping of 6.90 at% exhibits an excellent ORR activity with an onset potential of 0.95 V *vs.* RHE and a diffusion-limited current of 6.82 mA cm^{-2}. This ORR performance is superior to that of the commercial Pt/C catalyst (0.94 V, 4.94 mA cm^{-2}) and other reported N doped CNTs in alkaline media. The extraordinary long-term stability and tolerance against methanol corrosion would guarantee its potential applications such as full cells and metal–air batteries.

Acknowledgements

This work was supported by the National Natural Science Foundation of China (NSFC), the 973 Program (Grant No. 2014CB932102) and the Fundamental Research Funds for the Central Universities (buctrc201506; YS 1406). M. Wei particularly appreciates the financial aid from the China National Funds for Distinguished Young Scientists of the NSFC.

Notes and references

1 Y. H. Bing, S. Liu, L. Zhang, D. Ghosh and J. J. Zhang, *Chem. Soc. Rev.*, 2010, **39**, 2184.
2 Y. Zheng, Y. Jiao, M. Jaroniec, Y. Jin and S. Z. Qiao, *Small*, 2012, **8**, 3550.
3 B. Lim, M. Jiang, P. H. C. Camargo, E. C. Cho, J. Tao, X. Lu, Y. Zhu and Y. Xia, *Science*, 2009, **324**, 1302.
4 H. Liang, X. Cao, F. Zhou, C. Cui, W. Zhang and S. Yu, *Adv. Mater.*, 2011, **23**, 1467.
5 S. Guo and S. Sun, *J. Am. Chem. Soc.*, 2012, **134**, 2492.
6 C. Wang, H. Daimon, T. Onodera, T. Koda and S. Sun, *Angew. Chem., Int. Ed.*, 2008, **47**, 3588.
7 N. Kakati, J. Maiti, S. H. Lee, S. H. Jee, B. Viswanathan and Y. S. Yoon, *Chem. Rev.*, 2014, **114**, 12397.
8 Q. S. F. Peng, S. Liao, H. Wang, H. Yu, Z. Liu, B. Zhang and D. Su, *J. Mater. Chem. A*, 2013, **1**, 14853.
9 W. Yang, X. Liu, X. Yue, J. Jia and S. Guo, *J. Am. Chem. Soc.*, 2015, **137**, 1436.
10 S. Chen, J. Bi, Y. Zhao, L. Yang, C. Zhang, Y. Ma, Q. Wu, X. Wang and Z. Hu, *Adv. Mater.*, 2012, **24**, 5593.
11 C. Cao, L. Wei, M. Su, G. Wang and J. Shen, *J. Mater. Chem. A*, 2016, **4**, 9303.
12 Y. Zheng, Y. Jiao, J. Chen, J. Liu, J. Liang, A. Du, W. Zhang, Z. Zhu, S. Smith, M. Jaroniec, G. Q. Lu and S. Z. Qiao, *J. Am. Chem. Soc.*, 2011, **133**, 20116.
13 J. Liu, H. Yang, S. G. Zhen, C. K. Poh, A. Chaurasia, J. Luo, X. Wu, E. K. L. Yeow, N. G. Sahoo, J. Lin and Z. Shen, *RSC Adv.*, 2013, **3**, 11745.
14 K. Meng, Q. Liu, Y. Huang and Y. Wang, *J. Mater. Chem. A*, 2015, **3**, 6873.
15 C. Hu, C. Yu, M. Li, X. Wang, Q. Dong, G. Wang and J. Qiu, *Chem. Commun.*, 2015, **51**, 3419.
16 L. Wang, J. Yin, L. Zhao, C. Tian, P. Yu, J. Wang and H. Fu, *Chem. Commun.*, 2013, **49**, 3022.
17 R. Ning, J. Tian, A. M. Asiri, A. H. Qusti, A. O. Al-Youbi and X. Sun, *Langmuir*, 2013, **29**, 13146.
18 R. Ning, C. Ge, Q. Liu, J. Tian, A. M. Asiri, K. A. Alamry, C. M. Li and X. Sun, *Carbon*, 2014, **78**, 60.
19 T. N. Tran, M. Y. Song, K. P. Singh, D. S. Yang and J. S. Yu, *J. Mater. Chem. A*, 2016, **4**, 8645.
20 G. L. Tian, Q. Zhang, B. S. Zhang, Y. G. Jin, J. Q. Huang, D. S. Su and F. Wei, *Adv. Funct. Mater.*, 2014, **24**, 5956.
21 Z. H. Li, M. F. Shao, L. Zhou, R. K. Zhang, C. Zhang, M. Wei, D. G. Evans and X. Duan, *Adv. Mater.*, 2016, **28**, 2337.
22 J. Tian, R. Ning, Q. Liu, A. M. Asiri, A. O. Al-Youbi and X. Sun, *ACS Appl. Mater. Interfaces*, 2014, **6**, 1011.
23 S. Yasuda, A. Furuya, Y. Uchibori, J. Kim and K. Murakoshi, *Adv. Funct. Mater.*, 2016, **26**, 738.
24 J. Liu, L. Lai, N. G. Sahoo, W. Zhou, Z. Shen and S. H. Chan, *Aust. J. Chem.*, 2012, **65**, 1213.
25 K. Gong, F. Du, Z. Xia, M. Durstock and L. M. Dai, *Science*, 2009, **323**, 760.
26 D. Yu, Q. Zhang and L. M. Dai, *J. Am. Chem. Soc.*, 2010, **132**, 15127.
27 Z. Wang, R. Jia, J. Zheng, J. Zhao, L. Li, J. Song and Z. Zhu, *ACS Nano*, 2011, **5**, 1677.
28 C. V. Rao, C. R. Cabrera and Y. Ishikawa, *J. Phys. Chem. Lett.*, 2010, **1**, 2622.
29 R. Du, N. Zhang, J. Zhu, Y. Wang, C. Xu, Y. Hu, N. Mao, H. Xu, W. Duan, L. Zhuang, L. Qu, Y. Hou and J. Zhang, *Small*, 2015, **11**, 3903.
30 D. S. Yu, Y. H. Xue and L. M. Dai, *J. Phys. Chem. Lett.*, 2012, **3**, 2863.
31 P. Chen, T. Y. Xiao, Y. H. Qian, S. S. Li and S. H. Yu, *Adv. Mater.*, 2013, **25**, 3192.
32 Q. Zhang, J. Q. Huang, M. Q. Zhao, W. Z. Qian, Y. Wang and F. Wei, *Carbon*, 2008, **46**, 1152.
33 Y. Zheng, Y. Jiao, M. Jaroniec, Y. Jin and S. Z. Qiao, *Small*, 2012, **8**, 3550.
34 J. Sun, H. Liu, X. Chen, D. G. Evans, W. Yang and X. Duan, *Adv. Mater.*, 2013, **25**, 1125.
35 C. Tang, H. Wang, X. Chen, B. Li, T. Hou, B. Zhang, Q. Zhang, M. Titirici and F. Wei, *Adv. Mater.*, 2016, **28**, 6845.
36 W. Wei, H. W. Liang, K. Parvez, X. D. Zhuang, X. L. Feng and K. Müllen, *Angew. Chem.*, 2014, **126**, 1596.

37 W. Zhang, Z. Wu, H. Jiang and S. Yu, *J. Am. Chem. Soc.*, 2014, **136**, 14385.

38 D. H. Guo, R. Shibuya, C. Akiba, S. Saji, T. Kondo and J. Nakamura, *Science*, 2016, **351**, 361.

39 Z. W. Chen, D. Higgins, A. P. Yu, L. Zhang and J. J. Zhang, *Energy Environ. Sci.*, 2011, **4**, 3167.

40 L. Lin, Q. Zhu and A. W. Xu, *J. Am. Chem. Soc.*, 2014, **136**, 11027.

41 W. Xia, A. Mahmood, R. Zou and Q. Xu, *Energy Environ. Sci.*, 2015, **8**, 1837.

42 H. Zhong, J. Wang, Y. Zhang, W. Xu, W. Xing, D. Xu, Y. Zhang and X. Zhang, *Angew. Chem., Int. Ed.*, 2014, **53**, 14235.

43 T. Xing, Y. Zheng, L. H. Li, B. C. C. Cowie, D. Gunzelmann, S. Z. Qiao, S. M. Huang and Y. Chen, *ACS Nano*, 2014, **8**, 6856.

44 Y. Chen, C. Wang, Z. Wu, Y. Xiong, Q. Xu, S. Yu and H. Jiang, *Adv. Mater.*, 2015, **27**, 5010.